World Scientific
www.worldscientific.com

Hydrodynamic Study and Performance Analysis of the OC4-DeepCWind Platform by CFD Method

Yang Huang, Yuan Zhuang and Decheng Wan*

Computational Marine Hydrodynamics Lab (CMHL)
State Key Laboratory of Ocean Engineering
School of Naval Architecture, Ocean and Civil Engineering
Shanghai Jiao Tong University, Shanghai 200240, P. R. China
*dcwan@sjtu.edu.cn

(1) The RAOs of OC4-DeepCWind platform motions are more sensitive to the low-frequency wave than the high-frequency wave. The nonlinear motion responses for platform heave and pitch motions are comparatively remarkable.

(2) The pitch motion of OC4-DeepCWind platform is much more apparently influenced by the height of center of gravity (COG) than surge and heave motions. The lower COG height within a suitable range leads to a smaller fluctuation amplitude of platform pitch motion in waves.

(3) A large horizontal displacement abruptly occurs to the OC4-DeepCWind platform when one mooring line is failure. The risk of failure for the other mooring lines significantly increases.

To better understand the hydrodynamic performance of a floating support platform in various wave environments, a two-phase CFD solver naoe-FOAM-SJTU based on the open source CFD toolbox OpenFOAM is applied to investigate the hydrodynamic characteristics and motion performance of the OC4-DeepCWind platform. Moreover, the restoring force and moment of mooring lines are simulated using the solver in time domain. The studies of grid sensitivity and time step refinement are first conducted to determine an appropriate time step and mesh size. Then hydrodynamic responses of the floater in free-decay tests are analyzed and compared with experimental data, and the motion performance of the platform in regular waves with different parameters is also investigated. In addition, the platform motion responses with one mooring line broken and different heights of center of gravity are explored. It is shown that simulation results have good agreement with published data, and several conclusions can be drawn through the study. The RAOs of platform motions are found to be more sensitive to the low-frequency wave than the high-frequency wave. Nonlinear motion responses are comparatively remarkable in platform heave and pitch motions. Besides, the lower height of center of gravity within a suitable range is benefit to the stability of floating platform. Survival condition with broken mooring line should be paid enough attention to avoid the failure of other mooring lines.

Keywords: Semi-submersible platform; hydrodynamic characteristics; center of gravity; broken mooring line; naoe-FOAM-SJTU solver.

1. Introduction

With the deterioration of energy crisis and environmental issues like global warming, the exploration for clean renewable energies has become crucial. Various potential resources including the wind, wave, solar and tidal attract more and more attention. Numerous researchers are devoted to the research of these new energy resources [Yu *et al.* (2015)]. In recent years, wind power is one of the fastest growing renewable clean energy resources [Tang *et al.* (2015)]. Due to the limited onshore wind resource and space, wind power industry is advancing from the land to offshore area [Sun *et al.* (2012)]. The floating offshore wind turbines (FOWTs) gradually become the focus of the offshore wind energy research. The FOWT is a complicated system composed of a wind turbine, a floating support platform and a mooring system. Due to the coupling effects between the wind turbine and the floating support platform, it is challengeable to accurately predict coupled aero-hydrodynamic performance of the FOWT in realistic ocean environments [Tran and Kim (2015)]. The wind turbine mounted on the floating support platform experiences additional six degree-of-freedom (6DOF) motions, leading to significant variation of aerodynamic loads, severe fatigue loads and ultimate loads at the tower bottom and blade root [Yang *et al.* (2015)]. The aerodynamic loads further disturb the dynamic motion responses of the floating platform. The motion responses of the floating support platform have great impacts on the aerodynamic performance of the FOWT as well as the electricity generating capacity [Zhao *et al.* (2016)].

The concept of FOWT has been proposed for decades, a number of methods based on different theories have been applied to investigate the hydrodynamic characteristics of floating support platform of the FOWT. Based on the experience of offshore oil and gas development platform, hydrodynamic performance of a floating support platform is initially predicted by Morison equation [Zhang and Zhou (2002)]. This is a semi-empirical formula for calculating the wave forces acting on the platform, which is suitable for the hydrodynamic calculation of small-sized components with relatively simple cross-section [Lee and Incecik (2005)]. In addition, this method was further developed to calculate the hydrodynamic forces acting on the structures with arbitrary shape of the cross-section [Yong-Pyo *et al.* (2005)]. Besides, considering that coefficient-based engineering models have a long history of application in the hydrodynamic analysis of floating offshore structure [Jonkman (2007)], these models with simplified assumptions are also utilized to predict the hydrodynamic performance of the FOWT [Butterfield *et al.* (2007)].

Moreover, the potential-based panel approaches, which have advantages of simple form and fast calculation, are employed to predict the hydrodynamic performance of the floating structures. By incorporating the fluid effects on floating structures via various coefficients (such as added mass coefficient, damping coefficient, restoring coefficient), the buoyancy force, wave excitation force, damping effects and even viscous effects can all be considered in these simplified analysis methods [Fossen (2011); Vugts (1968)]. A number of software packages (such as AQWA,

ANSYS [Inc. (2012)], WAMIT [Lee and Newman (2006)], FAST [Jonkman (2013); Jonkman and Buhl (2005)], Orcaflex [Orcina (2015)]) were developed for time- and frequency-domain analysis of floating structures. These software packages have been widely validated and applied in the engineering field. However, some complicated physical phenomena including the wave run-up against the semi-submersible platform columns [Shan *et al.* (2011); Diaconu (2013)] and viscous effects on the floater cannot be adequately captured by the potential-based panel method due to the simplification of hydrodynamics. Additionally, the simulation results obtained from the software should be validated by experimental data [Huijs *et al.* (2014)].

The model experiment is believed to be one of the most convincing approaches to study the hydrodynamic performance of a floating platform. A lot of scale model tests [Naqvi (2012); Koo *et al.* (2014); Perez (2014); Sandner *et al.* (2015)] were carried out to investigate the hydrodynamic characteristics of various floating platforms. It is noted that the scale effects cannot be avoided in the model experiment. Compared with experimental tests, the computational fluid dynamic (CFD) method inherently satisfies the essential scaling laws. All physical phenomena, such as the flow viscosity, hydrostatic, wave diffraction, radiation, wave run-up and slamming, can all be modeled with the CFD method, which makes it is an advisable choice for hydrodynamic simulations of the floating platform. The CFD technology has been widely applied in hydrodynamic analyses of the floating platform. Zhao and Wan [2015] investigated the influence of aerodynamic loads on motion responses of the semi-submersible platform applied in Offshore Code Comparison Collaboration Continuation (OC4) project using in-house CFD code. Tran and Kim [2015] studied the hydrodynamic performance of the same platform using both panel method and CFD method. A tightly coupled 6-DOF solver based on the popular open source toolbox OpenFOAM was developed and validated by Dunbar *et al.* [2015], which was applied to carry on the simulation of floating structures. Burmester *et al.* [2017, 2018] analyzed the hydrodynamic characteristics of a semi-submersible floating platform. Liu *et al.* [2017] also investigated the motion responses of this floating platform using CFD method.

In order to better understand the hydrodynamic performance of the floating support platform, the hydrodynamic characteristics of a typical semi-submersible platform with a mooring system under regular wave conditions are investigated in this paper. Hydrodynamic analyses of the selected platform in time domain are conducted by a two-phase CFD solver naoe-FOAM-SJTU [Shen *et al.* (2012); Cao and Wan (2014); Cao *et al.* (2013); Zhao and Wan (2015); Cheng *et al.* (2019)] developed based on OpenFOAM. First of all, the studies of grid sensitivity and time step refinement are conducted to determine an appropriate time step and mesh size. Then free-decay motion tests for the selected platform in different DOFs are performed to prove the reliability and accuracy of present computational model. The free-decay motion characteristics are also compared with the experimental data. After that, the hydrodynamic performance of the floating platform in various regular

waves is predicted by naoe-FOAM-SJTU solver. Comparisons for platform motion responses obtained from experiment, CFD method and FAST code are achieved. Moreover, the influence of the height of center of gravity (COG) on platform motion responses is discussed.The dynamic responses of the floating platform with one mooring line broken are also investigated. Finally, several conclusions are drawn from the results and discussions.

2. Simulation Methods

The two-phase CFD solver naoe-FOAM-SJTU is based on a built-in solver named interDyFoam in OpenFOAM. This solver can be applied to the incompressible, isothermal and immiscible two-phase flow problem. To handle common fluid–structure interaction problems in ship hydrodynamics and offshore engineering, several modules, such as a wave generation/damping module, a 6-DOF motion module and a mooring system module, are further developed and integrated into naoe-FOAM-SJTU solver.This solver can be applied to predict the hydrodynamic performance of various floating structures in wave environments [Wang and Wan (2018); Wang *et al.* (2019); Zhuang and Wan (2019)].

2.1. *Governing equations*

The Navier–Stokes equations are selected as governing equations to solve the transient, incompressible and viscous fluid flow problems in the present work [Shen *et al.* (2012); Wang *et al.* (2019)], which can be written as follows:

$$\nabla \cdot U = 0, \tag{1}$$

$$\frac{\partial \rho \mathbf{U}}{\partial t} + \nabla(\rho(\mathbf{U} - \mathbf{U}_g)\mathbf{U}) = -\nabla p_d - \mathbf{g} \cdot \mathbf{x}\nabla\rho + \nabla(\mu\nabla\mathbf{U}) + \mathbf{f}_\sigma + \mathbf{f}_s, \tag{2}$$

where $\mathbf{U}$ is the velocity field. $\mathbf{U_g}$ represents the velocity of mesh points. It should be noted that this velocity only has effects on the convection term. $p_d = p - \rho\mathbf{g}\cdot\mathbf{x}$ is the dynamic pressure by subtracting the hydrostatic part from total pressure p. $\mathbf{g}$ is the gravity acceleration vector. ρ is the mixture density with two phases. $\mu = \rho(\nu + \nu_t)$ denotes the effective dynamic viscosity, in which ν and ν_t are kinematic viscosity and eddy viscosity, respectively. $\mathbf{f}_\sigma$ is the surface tension term in two-phase flow model and takes effect only on the liquid-free surface. $\mathbf{f}_s$ is the source term for the sponge layer, which is set to absorb the wave reflection and takes effect only in the sponge layer.

A volume-of-fluid (VOF) method with bounded compression technique is applied to capture the water surface [Rusche (2002); Berberović *et al.* (2009)]. Considering that there is no explicit coupling between velocity and pressure in Navier–Stokes equations, a segregated method named PIMPLE is employed to couple the governing equations with an iterative procedure. PIMPLE is a combination of Pressure-Implicit with Splitting of Operations (PISO) algorithm and Semi-Implicit Method

for Pressure-Linked Equations (SIMPLE) [Issa (1986)]. Detailed calculation procedure of PIMPLE algorithm has been illustrated in the previous study [Wang *et al.* (2019)]. Besides, the governing equations are discretized by finite volume method (FVM) [Eymard *et al.* (2000)]. The convection terms are solved by a second-order TVD limited linear scheme, and the diffusion terms are approximated by a second-order central difference scheme. A second-order backward method is used for time discretization. Moreover, the van Leer scheme [Van Leer (1979)] is used to discretize the VOF transport equation.

Due to the huge inertia of floating platform, the motion responses of floating platform under given regular wave conditions are relatively small, and the flow around the surface of floating platform is smooth. The largest Reynolds number of the base column is about 26,000 in surge free-decay motion. It means that the surrounding flow of the platform can be assumed to be laminar. Thus, a laminar model is selected in this study, and turbulence is not modeled in numerical simulations. It is shown that the laminar model can give relatively accurate results of hydrodynamic responses of platform under low Reynolds number flow [Kim *et al.* (2011); Tran and Kim (2015)].

2.2. *Wave generation/damping*

Various types of waves can be generated with the wave generation module of naoe-FOAM-SJTU solver. The first-order stokes wave and second-order stokes wave are adopted in this paper. The wave elevation η is defined by the following equation [Lin and Liu (1999)]:

$$\eta = A\cos(kx - \omega t), \tag{3}$$

$$\eta = a_1 \cos(kx - \omega t) + a_2 \cos 2(kx - \omega t), \tag{4}$$

where A denotes the wave amplitude. ω is the wave angular frequency. k represents the wave number. a_1 is the amplitude of the first-order item, and the a_2 is the amplitude of the second-order item.

To avoid interactions between the incident wave and the reflected wave, a rectangular sponge layer located before the outlet boundary is adopted to absorb wave
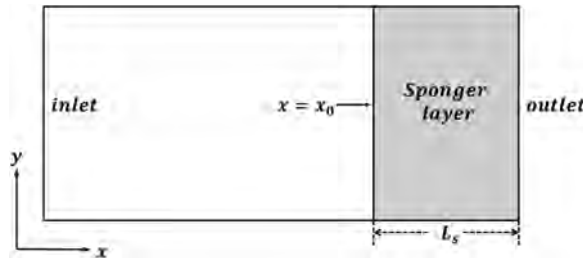

Fig. 1. Overlooking of the computational domain and sponge layer.

reflection, as shown in Fig. 1. The sponge layer takes effect by adding an additional artificial viscous term to right-hand side of the momentum equation [Ohyama and Nadaoka (1991); Zhuang and Wan (2019)]. This source term is expressed as

$$\mathbf{f}_s = -\rho\mu_s\mathbf{U}, \tag{5}$$

where μ_s is the artificial viscosity calculated by the following equation:

$$\mu_s(x) = \begin{cases} \alpha_s\left(\dfrac{x-x_0}{L_s}\right)^2, & x > x_0, \\ 0, & x \le x_0, \end{cases} \tag{6}$$

where α_s is a dimensionless quantity defining damping strength for the sponge layer. L_s is the length of the sponger layer.

A regular wave with wave period of 12.1 s and wave amplitude of 5.15 m is generated by the wave generation module of naoe-FOAM-SJTU solver. As shown in Fig. 2, the wave elevation modeled by this solver is compared with theoretical value. At the beginning of wave generation, there is small discrepancy in the period between the simulation result and theoretical value. After about 100 s, the comparison results show good agreement.

2.3. 6*DOF platform motions*

A 6DOF motion module based on Euler angle description is employed to estimate the motion responses of the floating platform in waves. Two coordinate systems are unitized in the calculation of platform motions, as shown in Fig. 3. The displacements and rotations of floating platform in earth-fixed coordinate system are defined
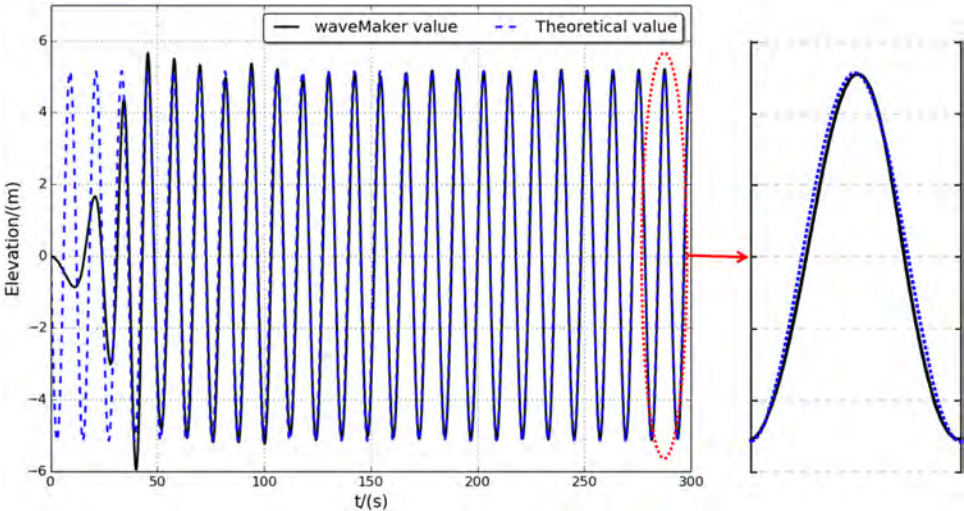

Fig. 2. Comparison between theoretical waveform and generated waveform by wave maker.
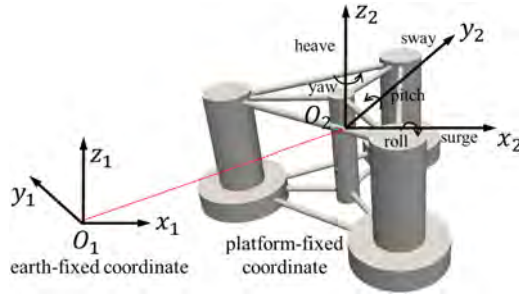
Fig. 3. Coordinate systems for 6DOF motion module.

as $\boldsymbol{\eta} = (\boldsymbol{\eta}_1, \boldsymbol{\eta}_2) = (x_1, x_2, x_3, \phi, \theta, \psi)$, donating motions of surge, sway, heave, roll, pitch and yaw, respectively. The linear and angular velocities in platform-fixed system are represented by $\boldsymbol{\nu} = (\boldsymbol{\nu}_1, \boldsymbol{\nu}_2) = (u, v, w, p, q, r)$. The velocities in two coordinate systems can be converted to each other through transformation matrices depending on Euler angles.

It is noted that forces on each cell face of the platform surface including the viscous force and pressure are first computed in earth-fixed coordinate system. The total forces and moments acting on floating platform hull are also integrated in the same coordinate system, including the gravity force. Then the forces and moments are projected into platform-fixed coordinate system. Linear and angular accelerations are determined by solving the motion equations, and velocities of the 6DOF motions in platform system can be obtained by the integration of accelerations with time. Next, these velocities are transformed into earth-fixed coordinate system. Finally, the motions of the floating platform can be obtained by integrating the velocities in earth-fixed coordinate system.

The motions of the floating platform are implemented by employing a moving-mesh technique. The dynamic deformation mesh is selected in the present work [Shen *et al.* (2012); De Boer *et al.* (2007)]. The topology of mesh does not change while the floating platform is moving, but only the spacing between nodes changes by stretching and squeezing and cell shape deforms. The positions of the mesh points in the field are determined by solving a Laplace equation with constant or variable diffusivity:

$$\boldsymbol{\nabla} \cdot (\gamma \boldsymbol{\nabla} \mathbf{U}_g) = 0, \tag{7}$$

where γ represents diffusivity field, which is based on the inverse square of the distance (r) between cell centers and moving boundary.

$$\gamma = \frac{1}{r^2}. \tag{8}$$

The Laplace equation can also be solved by the mesh displacement directly:

$$\boldsymbol{\nabla} \cdot (\gamma \boldsymbol{\nabla} \mathbf{X}_g) = 0, \tag{9}$$

where $\boldsymbol{X}_g$ is the displacement of mesh nodes.

2.4. *Mooring system*

The piecewise extrapolating method (PEM), which is a quasi-static mooring line analysis method, is employed in the present work to solve the constraint of the mooring line system [Fan *et al.* (2012); Liu *et al.* (2015); Cheng *et al.* (2019)]. In this method, a mooring line is divided into a series of segments. The length of segment is identical, and the number of segments can be defined. Static equilibrium analysis for a typical segment is shown in Fig. 4, and equations of static equilibrium are established in both horizontal and vertical directions [Liu *et al.* (2017)].

$$
\begin{cases}
T_{xi+1} = T_{xi} + F_i ds \cos \varphi_{i+1} + D_i ds \sin \varphi_{i+1}, \\
T_{zi+1} + D_i ds \cos \varphi_{i+1} = T_{zi} + F_i ds \sin \varphi_{i+1} + w_i dl,
\end{cases}
\tag{10}
$$

where T_x and T_z are the horizontal and vertical components of total mooring tension at a cross-section of one segment; φ is the angle between total tension force vector and horizontal plane; dl and ds are the segment lengths before and after elongation, respectively; w is the net submerged weight of lines per unit length; D and F denote normal and tangential components of drag force acting on the segment, which are calculated by Morison's equation.

The secant method with an iterative manner is used to calculate the mooring tension. Then the calculated mooring tensions are applied to the fairlead of floating platform. This is accomplished by adding the mooring forces into the 6DOF motion equations as an external mooring loading.

2.5. *Coupled simulation for platform hydrodynamics*

The solving produce of hydrodynamic simulation of the floating platform with mooring system in wave environments is presented in Fig. 5. An explicit coupling strategy is adopted to combine the 6DOF solver, RANS solver and mooring solver. At the
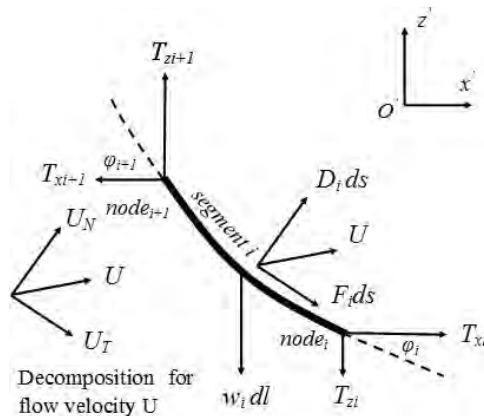

Fig. 4. Static equilibrium analysis for a typical segment in PEM.

```
          ┌─────────────────────────┐
          │    Start simulation     │
          └─────────────────────────┘
                      │
          ┌─────────────────────────┐
          │   Initialize flow field │
          └─────────────────────────┘
                      │
          ┌─────────────────────────┐
          │     New time step       │◄────────┐
          └─────────────────────────┘         │
                      │                        │
          ┌─────────────────────────┐         │
          │ Read mesh fluid fields  │         │
          │      & motions          │         │
          └─────────────────────────┘         │
                      │                        │
          ┌─────────────────────────┐         │
          │ Solve VOF transport eq. │         │
          └─────────────────────────┘         │
                      │                        │
          ┌─────────────────────────┐         │
          │ Solve RANS eq. w/ PIMPLE│         │
          └─────────────────────────┘         │
                      │                        │
          ┌─────────────────────────┐         │
          │ Calc mooring forces     │         │
          └─────────────────────────┘         │
                      │                        │
          ┌─────────────────────────┐         │
          │ Calc fluid forces       │         │
          └─────────────────────────┘         │
                      │                        │
          ┌─────────────────────────┐         │
          │ Solve 6DoF motion eq.   │         │
          └─────────────────────────┘         │
                      │                        │
          ┌─────────────────────────┐         │
          │ Solve deforming mesh    │         │
          └─────────────────────────┘         │
                      │          No            │
               < Last time step >──────────────┘
                      │ Yes
          ┌─────────────────────────┐
          │    End simulation       │
          └─────────────────────────┘
```
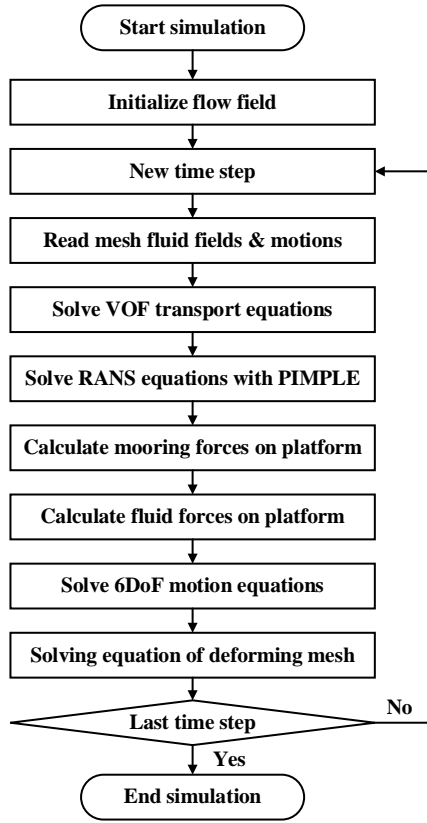
Fig. 5. Solving procedure of hydrodynamic simulation.

beginning of simulation, the flow field is initialized. In every time step, the first step is to read the flow field information and motions calculated from the previous time step. Then the VOF transport equations are solved. The next step is to calculate the pressure and velocity in the flow field with PIMPLE algorithm. After that, the fluid forces acting on floating platform are integrated over the surface of platform. The mooring forces can also be obtained by using the position of platform in the last time step. The 6DOF motion equations are solved with the second-order method adopted by OpenFOAM. The deforming mesh equation is subsequently solved with the predicted motion responses of the platform. Then the calculation advances to the next time step. It is reminded that the residuals of discrete terms in the governing equations are selected as the convergence criteria. The residuals of all discrete terms in governing equations including volume fraction, pressure and velocity are normalized using L2 norm, and these residuals should satisfy the tolerance. In the present simulations, the tolerance for volume fraction is set to $1e-10$, and tolerances for pressure and velocity are $5e-8$ and $1e-7$, respectively. In addition, the maximum number of iterations per time step is set to $1e3$.

3. Computational Model

3.1. *Platform parameter and mooring system configuration*

The OC4-DeepCWind platform with a catenary mooring system is selected as the analysis object in this study. This is a deep water semi-submersible platform designed for the FOWT, which is developed by the National Renewable Energy Laboratory (NREL). The platform is composed of three offset columns with larger diameter lower bases, one center support column for the wind turbine and a series of horizontal and diagonal cross bracings. It is noted that the diagonal cross bracings have little influence on the platform motions, and the platform is regarded as grid body. Moreover, a fine grid and a small time-step size are required to make the calculation converge when the diagonal cross bracings are considered. To balance the computational accuracy and computational time, the diagonal cross bracings are not taken into account. Similar simplification can also be found in the previous study [Liu *et al.* (2017)]. The geometry model of the OC4-DeepCWind platform is illustrated in Fig. 6(a), and main parameters are summarized in Table 1. The coordinate system of the platform is defined in Fig. 6(b).

(a) Platform geometry model (b) Coordinate system
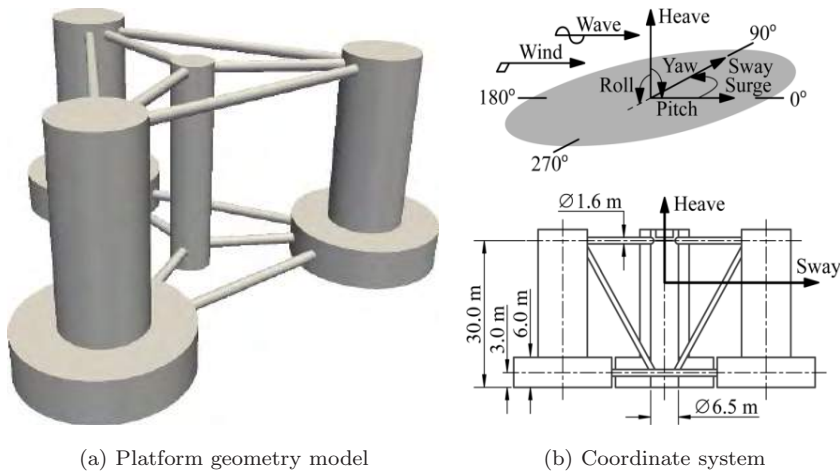
Fig. 6. Calculation model and coordinate setting [Coulling *et al.* (2013)].

Table 1. Gross parameters of the OC4-DeepCWind platform [Robertson *et al.* (2014)].

| Primary parameter	Unit	Value
Depth of platform base below SWL (total draft)	m	20
Elevation of main column (tower base) above SWL	m	10
Displacement	m3	13,986.8
Center of mass location below SWL along platform center line	m	14.4
Platform roll inertia about center of mass (CM)	$Kg \cdot m^2$	8.011×10^9
Platform pitch inertia about center of mass (CM)	$Kg \cdot m^2$	8.011×10^9
Platform yaw inertia about platform centerline	$Kg \cdot m^2$	81.391×10^{10}
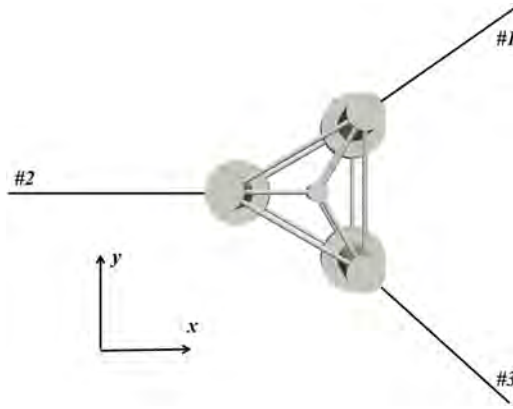
Fig. 7. Configuration of the mooring system around the platform.

To locate the floating platform and further limit the platform motions, the OC4-DeepCWind platform is moored by a mooring system composed of three catenary lines. As shown in Fig. 7, three mooring lines are evenly arranged around the platform with a mooring radius of 837.6 m and a water depth of 200 m. The angle between two adjacent mooring lines is 120°. The fairleads of all lines are positioned at the top of the base column. The primary parameters of the mooring system are listed in Table 2.

3.2. *Computational domain and boundary conditions*

A cuboid-shaped domain with the dimensions of $900\,\mathrm{m}(x) \times 400\,\mathrm{m}(y) \times 300\,\mathrm{m}(z)$ is created for hydrodynamic simulations of the floating platform in waves. Figure 8 shows the arrangement of computational domain. The platform is located at the origin of earth-fixed coordinate system, 300 m behind the inlet boundary. In addition, a rectangular sponge layer before the outlet boundary is adopted to absorb the wave reflection.

As shown in Fig. 9, different mesh resolutions are generated in the computational domain. The grid sizes of background mesh in x direction and y direction are both

Table 2. Primary parameters of the mooring system [Robertson *et al.* (2014)].

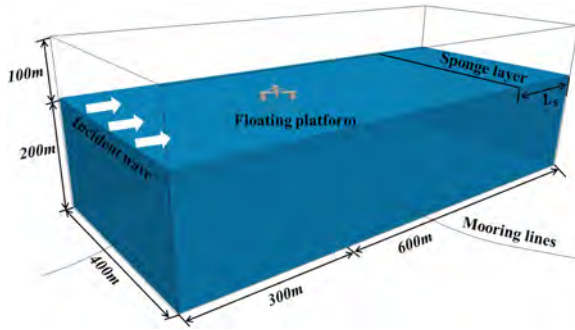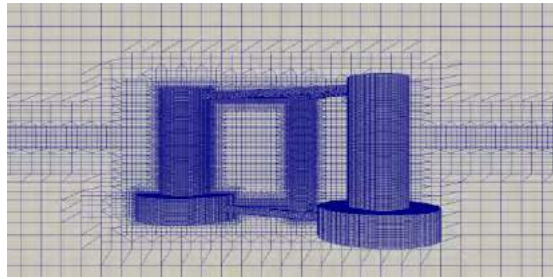| Primary parameter	Unit	Value
Number of mooring lines		3
Angle between adjacent lines	°	120
Depth to anchors below SWL (water depth)	M	200
Depth to fairleads below SWL	M	14
Radius to fairleads from platform centerline	M	4.0868
Radius to anchors from platform centerline	M	837.6
Equivalent mooring line mass in water	kg/m	108.63

Fig. 8. Configuration of the computational domain.

(a) Mesh of the computational domain   (b) Local view near the platform

Fig. 9. Computational domain and grid distribution.

8 m, while the grid sizes in negative and positive z directions both nonlinearly vary in order to limit the total grid number. The vertical size of grid near water surface is 2 m, and it expands up to 10 m and 20 m at top and bottom boundaries, respectively. The refined mesh is generated near the water surface to capture wave propagation. The grid size of refined mesh is $2\,\mathrm{m} \times 2\,\mathrm{m} \times 0.5\,\mathrm{m}$, which is fine enough to capture the liquid-free surface. Moreover, the grids near the platform are also refined. Therefore, the total grid number of computational domain is 1.6 million.

To achieve wave incident condition, regular wave is imposed at the inlet boundary for the water phase. Velocity inlet condition is adopted for the inlet boundary. The normal zero gradient condition is employed for the outlet boundary. Considering the bottom of computational domain is the water bottom, the no-slip condition is utilized in both the bottom boundary and platform surface. Besides, the symmetrical condition is applied to the side planes of computational domain.

4. Results and Discussions

4.1. *Convergence tests for grid and time-step size*

In order to eliminate the influence of time-step size on the simulation results, the time-convergence test is conducted before detailed hydrodynamic discussions. Four

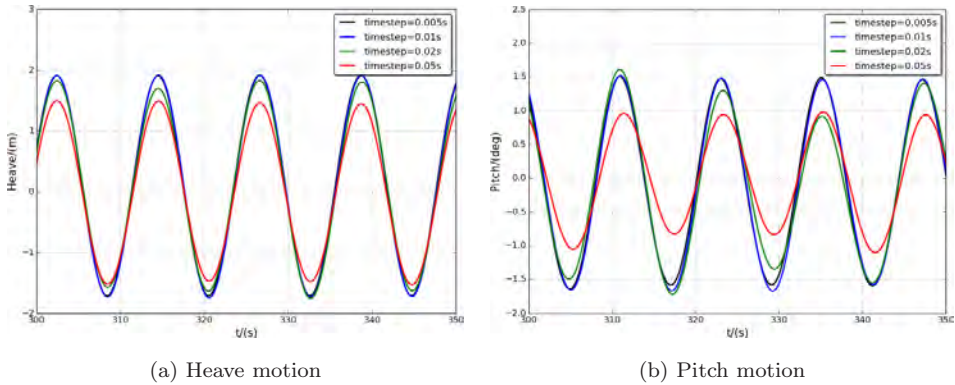(a) Heave motion   (b) Pitch motion

Fig. 10. Comparison of motion responses from time-step size convergence test.

different time-steps (0.005 s, 0.01 s, 0.02 s, 0.05 s) are selected. Time history curves of the platform motion responses under the same mesh condition but different calculation time-steps are compared and presented in Fig. 10. It is shown that the platform motions are sensitive to the time-step size. The motion amplitude with fine time-step is obviously larger than that with coarse time-step. This decrease of motion amplitude is mainly due to the "numerical damping" caused by improper computational setting, which leads to the inaccuracy of simulation results. The simulation results tend to be convergent with the decrease of time-step size. Moreover, the platform motion responses averaged from 300–350 s are listed in Table 3. It can be found that the motion responses with time-step size of 0.01 s are very close to those with 0.005 s. The comparison error is below 2%, indicating that the results are convergent with the time-step size of 0.01 s. To balance the computational accuracy and computation time, the time-step size of 0.01 s is selected for later numerical simulations.

Furthermore, three sets of grids with different resolutions are generated to perform grid convergence tests. The time-step size is set to 0.01 s, and wave parameters remain unchanged in the tests. Figure 11 shows the dynamic responses of heave and pitch motions from three sets of mesh. The dynamic motion responses of floating platform with different grid densities have similar variation trend, while the motion

Table 3. Platform motion responses in time-step convergence test.

Time-step (s)	Heave (m)		Pitch (degree)	
	Max.	Min.	Max.	Min.
0.005	1.905	−1.692	1.475	−1.597
0.01	1.919	−1.720	1.475	−1.640
0.02	1.797	−1.629	1.303	−1.522
0.05	1.479	−1.489	0.953	−0.953

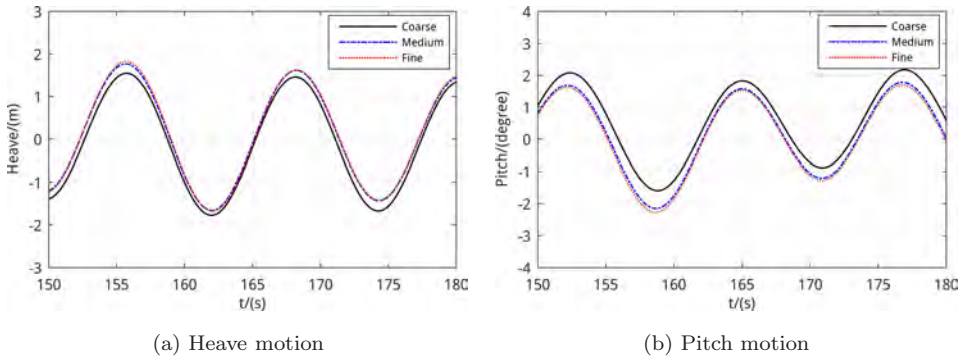(a) Heave motion   (b) Pitch motion

Fig. 11. Dynamic motion responses of floating platform from grid convergence test.

Table 4. RAOs of floating platform motions from grid convergence tests.

Grid	Grid number (million)	Heave (m/m)	Pitch($°$/m)
Coarse	1.0	0.322	0.332
Medium	1.6	0.333	0.363
Fine	3.5	0.340	0.370

amplitudes show notable discrepancy. The RAOs of floating platform from grid convergence tests are summarized in Table 4. The coarse grid contributes to the "numerical damping" and further increase the uncertainties of numerical simulations. It is seen that the differences for RAOs of heave and pitch motions between medium and fine mesh are both below 2%, indicating that comparative accurate results can be obtained with the medium mesh. Therefore, the medium mesh is chosen for the following numerical simulations.

4.2. *Free-decay motion of the platform*

Free-decay motion tests for the OC4-DeepCWind platform are conducted to demonstrate the reliability of computation set-up. In the free-decay simulation, the floating platform is initially placed at prescribed position, where the displacement is not equal to zero. Then the platform is released and move freely from the initial position. The initial position of the floating platform keeps the same with experimental data [Coulling *et al.* (2013)]. The wind and current speed both set to 0 m/s, and the fluid is absolutely static before the platform is released. In the present work, the free-decay motions along three different DOFs including surge, heave and pitch are simulated with naoe-FOAM-SJTU solver.

The dynamic surge and pitch responses of the OC4-DeepCWind platform in the free-decay motion tests are shown in Fig. 12. The CFD results calculated by naoe-FOAM-SJTU solver are compared with the other numerical results obtained from both CFD method and potential-flow method [SIMPACK (2013); Tran and

(a) Surge free-decay with 22 m initial displacement
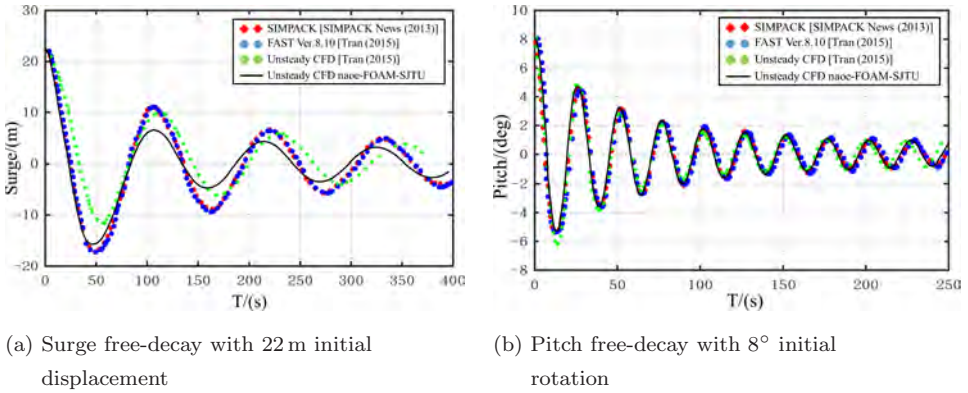

(b) Pitch free-decay with 8° initial rotation

Fig. 12. Comparison of free-decay motions of the OC4-DeepCWind platform.

Kim (2015)]. It can be seen that the present simulation results match well with other published numerical data, while small discrepancy is observed in the surge motion. It is seen that the magnitude of dynamic response of the floating platform predicted by unsteady CFD method is the lowest. This is an expected result that the CFD method is implemented to consider the effect of fluid viscosity. The main reason of this phenomenon is that the influence of fluid viscosity is omitted in hydrodynamic analyses of potential-flow based panel method, whereas CFD method inherently takes viscosity effects into consideration. In addition, coarse discretization in the CFD simulation leads to larger numerical diffusion and further results in the decrease of energy. The increase of "numerical damping" also contributes to this phenomenon.

The motion periods of the OC4-DeepCWind platform obtained from free-decay simulations are compared with experimental data [Coulling *et al.* (2013)] and published numerical results calculated by conventional software [Luan *et al.* (2013); Tran and Kim (2015)]. The comparison results are summarized in Table 5. To clearly illustrate the comparison error, the bar graph shown in Fig. 13 is also utilized. It is obviously seen that the present results based on unsteady CFD show a good agreement to the MARIN test data and other numerical results.

Table 5. Comparison of motion periods of the OC4-DeepCWind platform from free decay tests (Unit: s).

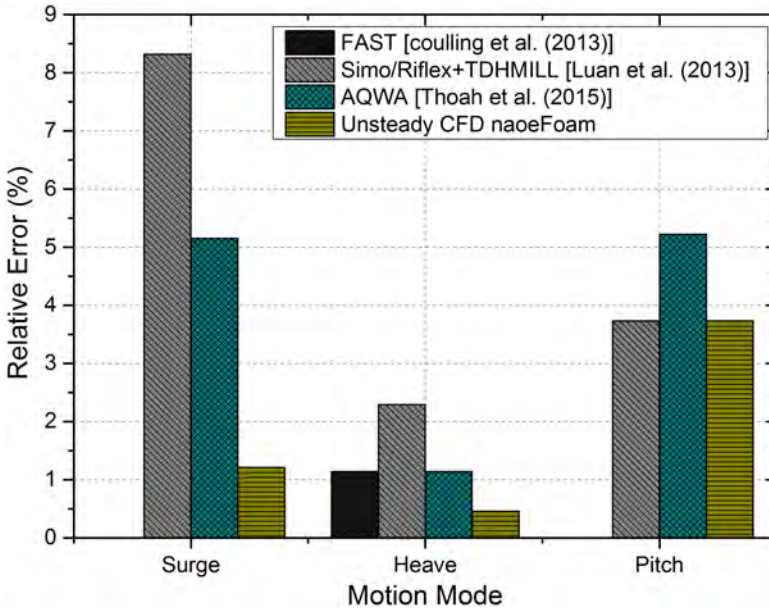| DOF	Experiment [Coulling *et al.* (2013)]	FAST [Coulling *et al.* (2013)]	Simo/Riflex+TDHMILL [Luan *et al.* (2013)]	AQWA [Tran and Kom (2015)]	CFD
Surge	107.0	107.0	115.9	112.5	108.3
Heave	17.5	17.3	17.1	17.3	17.58
Pitch	26.8	26.8	25.8	25.4	25.8

Fig. 13. Comparison of relative errors between several codes of the motion periods obtained from free-decay motions.

Compared with experimental data, the motion periods of the OC4-DeepCWind platform calculated by FAST [Coulling *et al.* (2013)] are the most accurate among all presented simulation results. The main reason is that the hydrodynamic coefficients adopted in FAST model are determined by the experimental data, such as the drag and inertia coefficients. Thus, even though the potential-flow based code was implemented in the simulations, the results are still the preeminent one. Except for the results obtained from FAST, the motion periods calculated by CFD method show lower comparison error than the other numerical results. It is noted that the numerical results calculated by CFD method and potential-flow based method all show evident disparate with experimental data. Some reasonable explanations are presented herein. On one hand, the uncertainty estimation is not conducted for model test data and numerical results, which leads to the considerable difference between numerical results and experimental data [Burmester *et al.* (2018)]. On the other hand, although the simulation and the physical experiment share the same experimental design and specifications, difference also exists which may be caused by the scale effect, mass distribution, structural flexibility of floating platform or different wave evolution in the process. Moreover, the OC4-DeepCWind platform utilized in the experiment is only an approximation model. The properties including the geometry, mass and inertia moment have a subtle difference with the design value [Coulling *et al.* (2013)]. Thus, small differences in the periods of free-decay motions are expected.
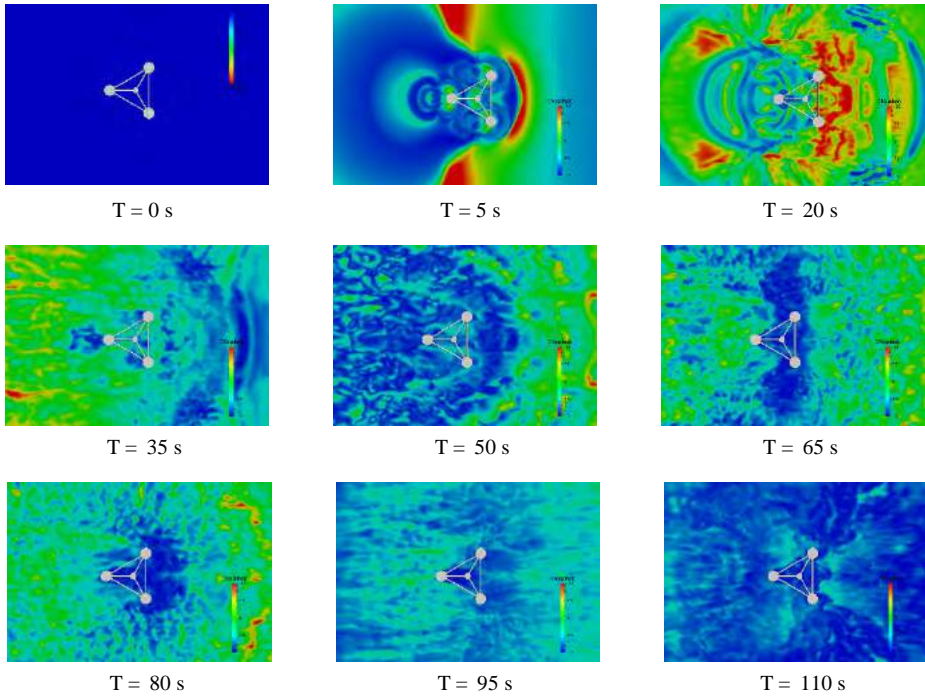
Fig. 14. Contour of velocity on the free surface in surge free-decay motion of the DeepCWind platform.

One of the advantages of CFD method is that detailed information of flow field can be obtained and visualized based on simulation results. Figure 14 shows the liquid-free surface colored by magnitude of velocity in surge free-decay motion. The liquid-free surface presented in Fig. 15 is colored by wave elevation. It is evident that both the velocity magnitude and the elevation of the free-surface are significantly affected by the motion responses. These impacts decrease with time due to the decay of surge displacement and surge velocity of floating platform. Generally, the results of free-decay motions prove that the current numerical model can accurately predict the hydrodynamic responses of the OC4-DeepCWind platform and can be applied for the following investigations.

4.3. *Hydrodynamic responses of the platform under regular wave conditions*

The dynamic responses of the OC4-DeepCWind platform under regular waves in the absence of wind are investigated in the present work. The regular waves with different amplitudes and periods are considered. Detailed wave parameters are listed in Table 6. All waves propagate in the positive surge direction. It is noted that two distinct amplitudes are investigated for periods of 14.3 s and 20.0 s for the purpose
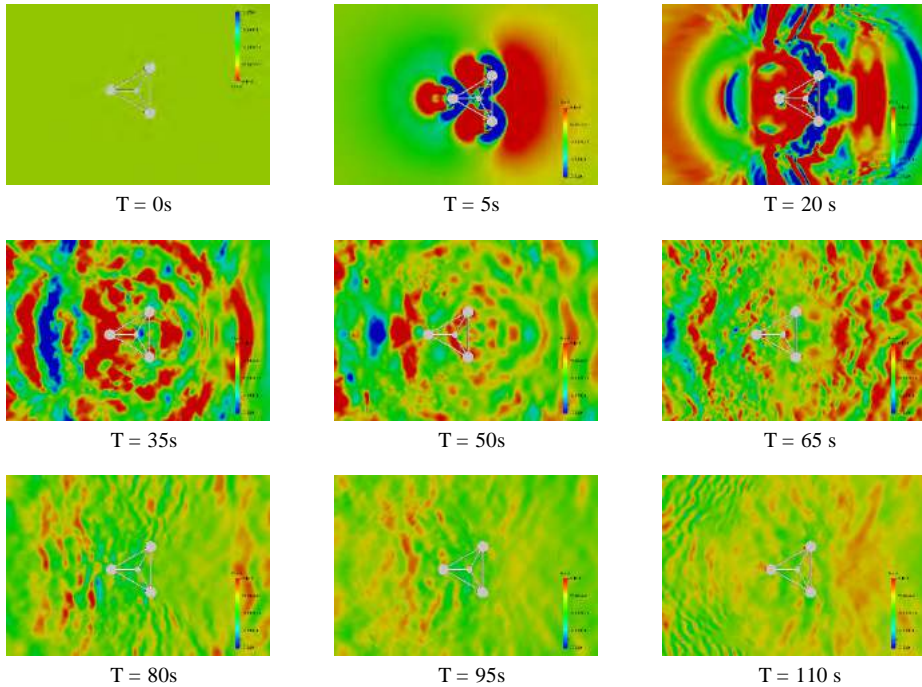
Fig. 15. Contour of magnitude elevation of the free surface of surge free-decay motion of the DeepCWind platform.

Table 6. Regular wave amplitudes and natural periods.

	Amplitude(m)	Period(s)
Case 1	3.57	14.3
Case 2	3.79	20
Case 3	5.15	12.1
Case 4	5.37	14.3
Case 5	5.56	20

of assessing the nonlinearity in system response. The motion performance of the OC4-DeepCWind platform is characterized by response amplitude operator (RAO) magnitudes, which normalize the amplitude of a periodic response of a field variable by the amplitude of regular waves [Coulling *et al.* (2013)]. According to the layout of the platform and wave direction, the wave forces acting on the platform are generally symmetry to *xz*-plane. It indicates that the sway, roll and yaw responses are small. Therefore, only the surge, heave and pitch responses are analyzed herein.

The hydrodynamic characteristics of the OC4-DeepCWind platform in regular waves have been investigated by calculation of RAO magnitudes. According to the guidelines of International Towing Tank Conference (ITTC), motion data should be

collected at least for 10 quasi-steady cycles under regular wave conditions to ensure the accuracy of results [ITTC (2002)]. Herein, the RAO values are calculated from the average value of nearly converged harmonic responses of the platform when the result is relatively steady.

The RAO magnitudes of different DOF responses (surge, heave and pitch) are presented in Fig. 16, which are compared with experimental data and numerical results calculated with FAST code [Coulling *et al.* (2013)]. Herein, the label of *x*-axis CASE is related to Table 6, which represents the different wave conditions considered in this paper.

The RAO magnitudes calculated by naoe-FOAM-SJTU solver show good agreement with experiment data, which are superior to the results of FAST. The large discrepancy between FAST results and experiment data is likely a result of the quadratic damping model employed in FAST. This model can properly model the damping for small to moderate motions, while it over-predicts the damping in large amplitude heave scenarios. The RAOs of platform motions under wave period of

(a) Surge motion   (b) Heave motion

(c) Pitch motion
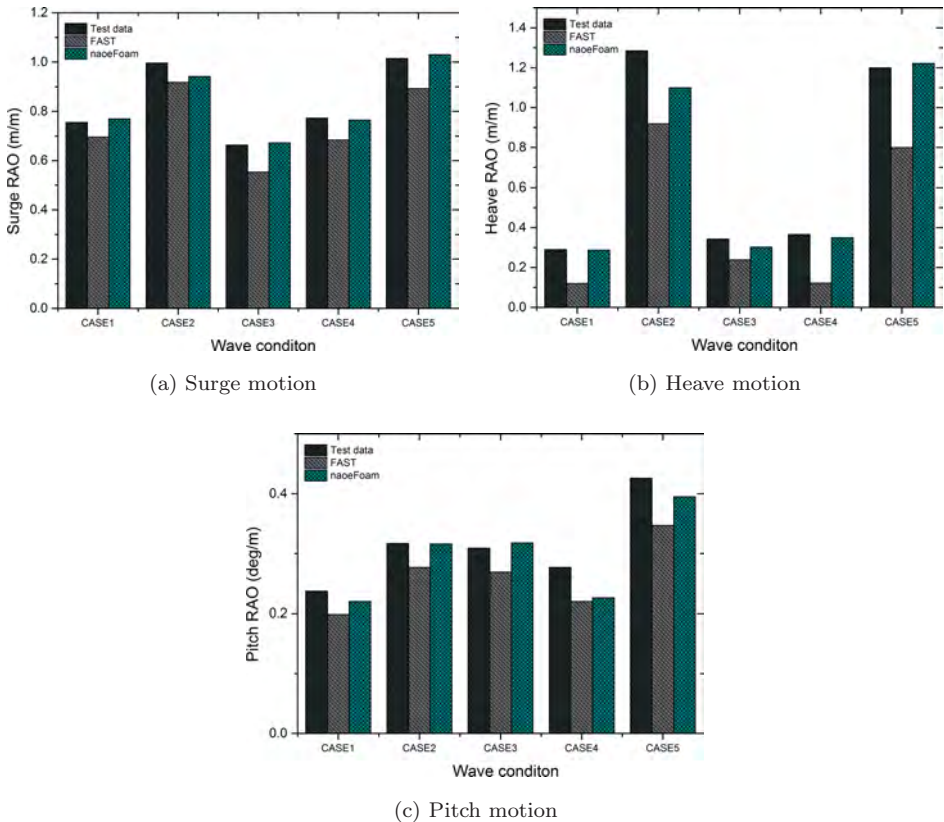
Fig. 16. Comparison of the calculated RAOs between experimental test, FAST and naoe-FOAM-SJTU.

20 s are obviously larger than those under wave periods of 12.1 s and 14.3 s. It indicates that the motion responses of floating platform are more sensitive to the low-frequency wave than the high-frequency wave. This is in-line with the findings of OC5 phase II group that the ultimate and fatigue loads of the floating platform in waves are severely underestimated in low-frequency region [Robertson *et al.* (2017)]. In addition, significant nonlinear phenomena are observed. The RAOs of platform motions under the same wave period but distinct wave amplitudes are different with each other, while these RAOs should be the same according to the linear theory regardless of the viscosity. These nonlinear phenomena are comparatively remarkable in platform heave and pitch motions, and they have significant effects on platform motion responses. It is noted that the fluid viscosity and the vortex are not directly considered in the potential-flow based panel codes, leading to the difficulty of confirming appropriate damping coefficient in numerical simulations. Furthermore, it results in the inaccuracy of the simulation results. In CFD method, the fluid viscosity and the vortex are inherently taken into consideration, so the nonlinear phenomena can be captured. As shown in Fig. 17, the vortex distributed on the surface of platform and the radiation of reflected wave induced by the platform motions are clearly observed. Moreover, some strong nonlinear problems, such as the wave run-up and the wave breaking, can also be satisfactorily solved by CFD method. Therefore, the CFD solver used in this paper is proved to be accurate enough in the predictions of hydrodynamic responses.

4.4. *Effect of the height of COG*

The height of COG is a key parameter for an offshore platform, which directly affects the stability of platform. At the same time, the COG height exactly influences the sea-keeping performance of the platform by affecting both the motion period and the motion amplitude. Furthermore, the stability of platform has significant impacts on the aerodynamic performance and power output of the FOWT. In order to ensure the stability of electricity generating of the FOWT, the amplitude of

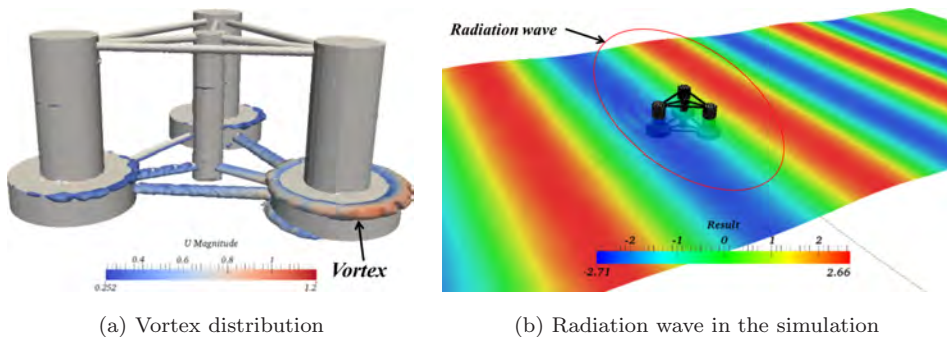(a) Vortex distribution   (b) Radiation wave in the simulation

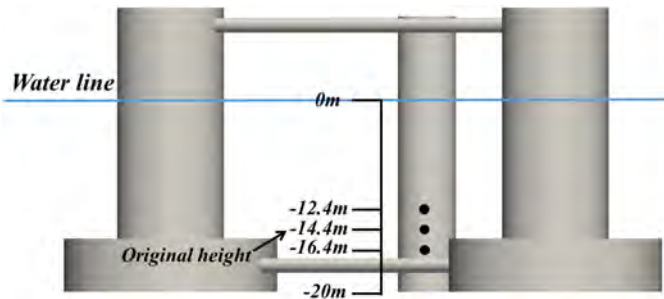Fig. 17. Vortex distribution and radiation wave induced by the platform motions during the simulation.

Fig. 18. Distribution of the height of COG.

platform motion should be as small as possible. Therefore, the influence of height of COG on the platform motions are investigated and evaluated in this section. Three different COG heights including the original designed value of 14.4 m are considered in the present simulations. The other values are −12.4 m and −16.4 m. The sketch of the distribution of different COG heights is shown in Fig. 18. A typical wave period of 12.1 s and relatively large wave amplitude of 5.15 m are chosen in the study of COG height, which refers to the previous study [Coulling *et al.* (2013)]. Comparisons of hydrodynamic responses of platform with different COG heights are achieved and presented in Fig. 19.

It is seen that the amplitudes of the platform surge and heave motions with different COG heights both show small change, indicating that the surge and heave motions are not sensitive to the height of COG. On the contrary, the fluctuating amplitude of the platform pitch motion greatly varies with the change of COG height. The pitch responses with the COG height of −16.4 m are almost the half of those with original COG height of −14.4 m. It is illustrated that the lower COG height within a suitable range is benefit to the stability of floating platform. An obvious reason for this phenomenon is that the stabilizing height of the platform increases with the decrease of COG height, and the static stability of the platform becomes better, resulting in the smaller amplitude of the platform pitch responses under given wave condition. In addition, a rational argument is that the influence of wave loads on the dynamic responses of the platform tends to be weaker with the position of COG becoming lower, which also leads to the decrease of the platform pitch responses.

The accelerations on top of the corner and center columns are illustrated in Fig. 20. It is interesting to find that the acceleration of the floating platform is reduced when the height of COG is located at a lower position. The acceleration is obtained by multiplying the angular acceleration with the distance between the measurement point and the COG. With the decrease of COG height, the distance from the top of corner column to platform COG becomes larger. However, the pitch angular acceleration significantly decreases when the height of COG is set to −16.4 m. The smaller acceleration makes it easier to maintain the floating support
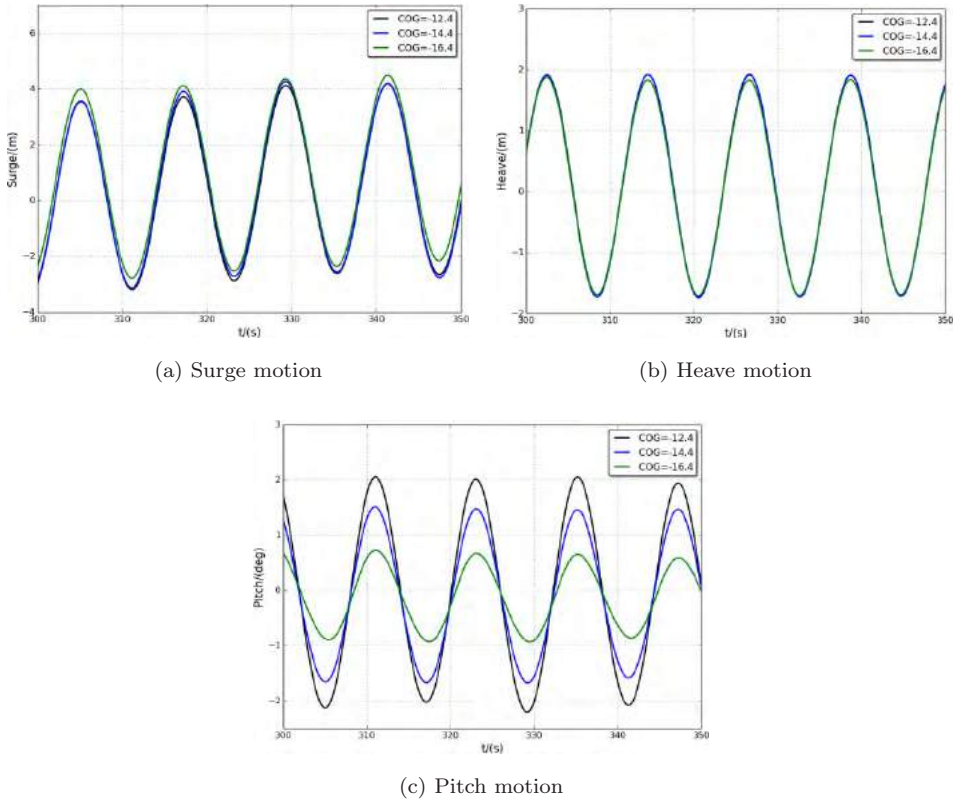
(a) Surge motion

(b) Heave motion

(c) Pitch motion

Fig. 19. Comparison of the motion responses of the platform with different COG heights.

(a) On the top of center column
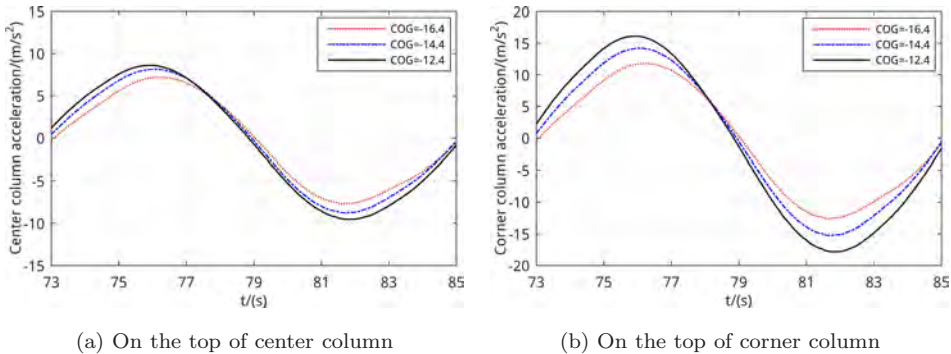
(b) On the top of corner column

Fig. 20. Accelerations of floating platform induced by the platform pitch motion.

platform, and it is also benefit to the steady operation of FOWT. However, it should be noted that the realistic mass distribution of FOWT is difficult to change, which raises a higher demand to the design of the floating platform. In addition, the variation of the height of COG also leads to the change of natural period of the

floating platform. According to the previous study [Rho *et al.* (2002)], the natural frequency will increase as the height of COG decreases. The natural frequency of the floating platform should be away from the range of typical wave frequency in realistic ocean environments in order to avoid the resonance, which should be considered in the design stage of the floating platform.

4.5. *One mooring line broken condition*

The mooring system plays a vital role in both operational and survival conditions of the floating platform, which not only maintains the position of the platform in horizontal direction but also provides restoring force and contributes to the stabilization of the platform. As illustrated in the previous work, the mooring tensions tend to become great with a large drift placement of the floating platform [Huang *et al.* (2019)]. Therefore, the failure of mooring line is considered in the present work. Simulations for the floating platform with one mooring line broken are conducted. The mooring line #3 is removed from the mooring system to represent the broken condition. It should be noted that the reason why chooses the mooring line #3 instead of the mooring line #2 is to make sure that the simulation for one mooring line broken condition can be successfully conducted. If the mooring line #2 is broken, the wave forces acting on the floating platform will be difficult to reach equilibrium. Thus, the floating platform is easy to capsize, leading to the divagation of hydrodynamic calculation. For the same purpose, the wave parameters are some what different from the previous condition. The wave amplitude is set to be 2.575 m, half of the wave amplitude in CASE 3, while the wave period remains the same (12.1 s). The configuration of the mooring system is shown in Fig. 21. Comparisons of the platform motion responses under broken condition (2 lines) and normal condition (3 lines) are achieved and illustrated in Fig. 22.

As shown in Fig. 22, the platform firstly experiences a significant surge displacement along the negative-x direction with a maximum value of about 15 m, and then it is pulled back along the positive-x direction to relative equilibrium
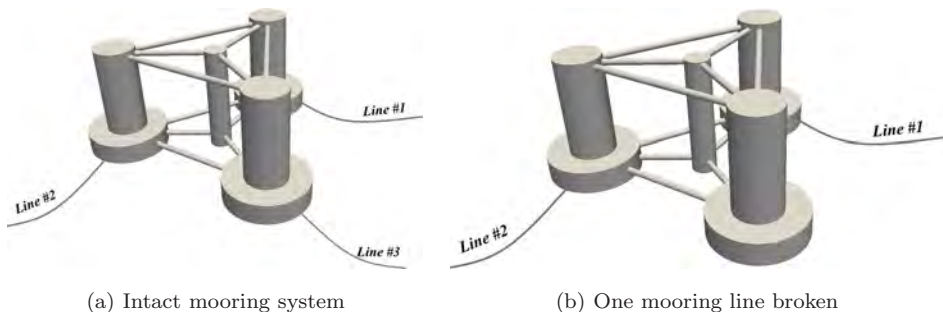

(a) Intact mooring system   (b) One mooring line broken

Fig. 21. Comparison of the arrangement of intact mooring system and one mooring line broken system.

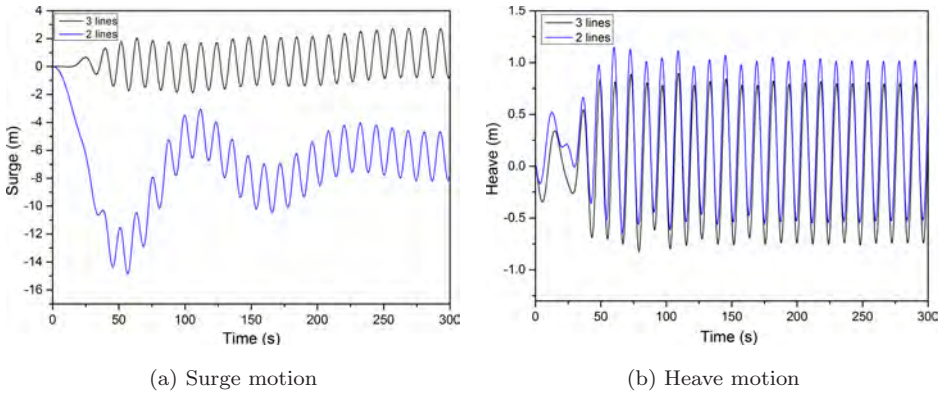| (a) Surge motion | (b) Heave motion |

Fig. 22. Comparison for motion responses between operational condition and survival condition.
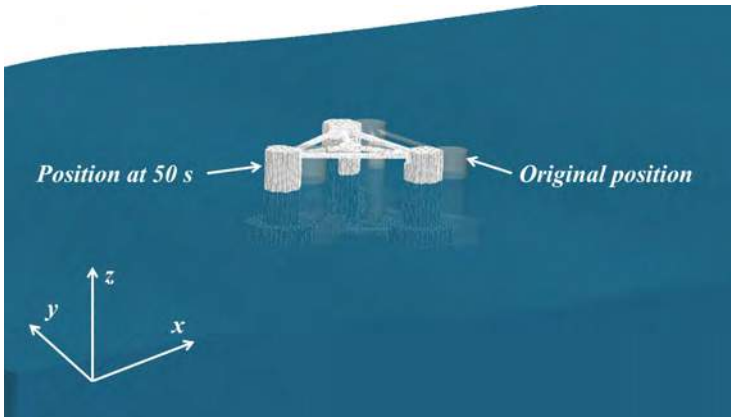

Fig. 23. Position of the platform at 50 s and 0 s.

position at about 7 m against the initial position. As presented in Fig. 23, the position of the platform at 50 s is compared with the original position. Subsequently, in the z-axis direction, the averaged heave displacement of the floating platform rises about 0.21 m after one mooring line is broken, which is induced by the lack of pretension force. Besides, the mooring forces of line #1 and line #2 are also investigated. As shown in Fig. 24, the blue line represents the survival condition with one mooring line broken, and the black line donates the operational condition with intact mooring system. It is easy to find that the averaged mooring force of line #1 becomes larger with the absence of line #3, while the averaged mooring force of line #2 obviously becomes smaller. Moreover, the oscillation amplitude of mooring force of line #1 also tends to increase, and the line #2 has the similar variation trend. The above phenomena indicate that the mooring tension of line #1 experiences a notable change. It means that the failure risk of line #1 is high and
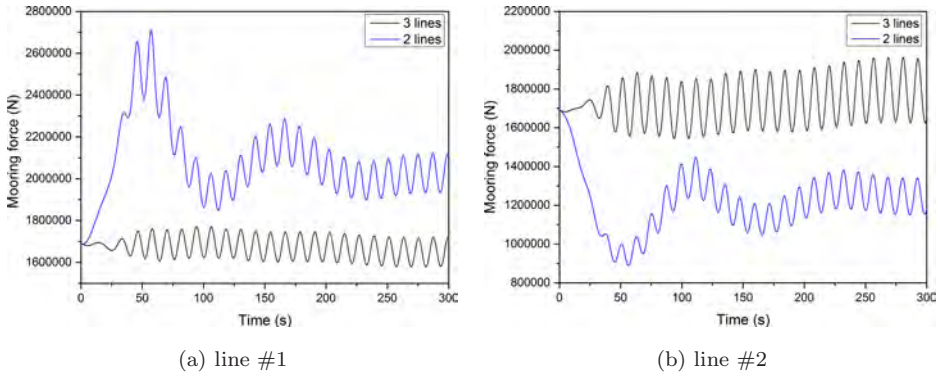
(a) line #1   (b) line #2

Fig. 24. Mooring forces of mooring line #1 and mooring line #2 in the different conditions.

more attention should be paid when the line #3 is broken.Additionally, it can be found that the total horizontal restoring force for the floating platform evidently reduces due to the lack of mooring line #3, resulting in the decrease of surge displacement. As presented in Fig. 22(a), the surge motion of the floating platform under one mooring line broken condition can be divided into two parts. One part is the wave frequency motion, and the other part is low-frequency motion related to the natural period of the platform. As analyzed in Sec. 4.2, the natural period of surge motion is about 107 s. However, the period of low-frequency surge motion with broken mooring line shown in Fig. 22(a) is obviously larger than this value. It is indicated that both the surge displacement and the period of surge motion are influenced by the horizontal restoring force provided by the mooring system.

5. Conclusion

In this study, a two-phase CFD solver naoe-FOAM-SJTU based on the open source toolbox OpenFOAM is applied to the hydrodynamic investigation of a typical semi-submersible platform named OC4-DeeCWind. The VOF method with boundary compressed technique is utilized to capture the free surface. The PIMPLE algorithm is employed to couple the governing equations with an iterative procedure. Hydrodynamic responses of the floating platform with mooring system in different regular waves are analyzed using CFD method. The free-decay motions along three different DOFs (surge, heave and pitch) predicted by naoe-FOAM-SJTU solver show good agreement with experimental data and other published numerical results, proving the reliability and accuracy of the present computational model. Additionally, compared with the potential-flow based method, CFD simulations are shown to have advantages of abundant flow-field information and more accurate simulation results.

The studies of grid sensitivity and time step refinement are firstly conducted to improve the quality and trustworthiness of simulation results. The appropriate time-step size and medium mesh are selected to balance the computational accuracy and computational time. Hydrodynamic analyses of the floating platform under

different regular waves are later carried out. The RAOs of platform motions (surge, heave and pitch) are compared with the numerical results calculated with FAST code and experimental data. The current results obtained from naoe-FOAM-SJTU solvers how good agreement with experimental data, indicating that this solver is accurate enough for hydrodynamic predictions of floating structures with mooring system in wave environments. Besides, the RAOs of platform motions are found to be more sensitive to the low-frequency wave than the high-frequency wave. The nonlinear motion responses are comparatively remarkable in platform heave and pitch motions.

Furthermore, the influence of COG height on motion responses of the floating platform and the dynamic responses of the floating platform with one mooring line broken is both investigated in detail. Several conclusions can be drawn from the results and discussions. Compared with surge and heave motions, platform pitch motion is much more sensitive to the height of COG. The lower COG height within a suitable range leads to a smaller fluctuation amplitude of platform pitch motion in waves, which is benefit to the stability of the floating platform. Besides, the decrease of the height of COG leads to the increase of natural frequency of the floating platform. When one mooring line is broken, the floating platform experiences an abruptly large horizontal displacement and a small water plane rise. The mooring tensions of other mooring lines also significantly change, and the failure risk of the other mooring lines significantly increases. It is also found that both the surge displacement and the period of surge motion are influenced by the horizontal restoring force provided by the mooring system. The present results contribute on the design and operation of the floating support platform. However, it should be noted that the wave conditions are limited to regular waves. The realistic sea environments are much more complicated than those in the present work. Thus, the hydrodynamic performance of the floating platform in various complicated environments will be further studied.

Acknowledgments

References

ANSYS, Inc. [2012] *275 Technology Drive, AQWA Reference Manual*, 14.5 Edition (ANSYS, Canonsburg).

Berberović, E., van Hinsberg, N. P., Jakirlić, S., Roisman, I. V. and Tropea, C. [2009] "Drop impact onto a liquid layer of finite thickness: Dynamics of the cavity evolution," *Phys. Rev. E* **79**(3), 036306.

Burmester, S., Gueydon, S., Vaz, G. and Moctar, B. [2017] "Surge decay simulations of a semi-submersible floating offshore wind turbine," *Proc. 20th Numerical Towing Tank Symp.*, 2–3.

Burmester, S., Vaz, G., Gueydon, S. and Moctar, O. [2018] "Investigation of a semi-submersible floating wind turbine in surge decay using CFD," *Ship Tech. Res.* 1–13.

Butterfield, C., Musial, W., Jonkman, J., Sclavounos, P. and Wayman, L. [2007] "Engineering challenges for floating offshore wind turbines,"

Cao, H. J. and Wan, D. C. [2014] "Development of multidirectional nonlinear numerical wave tank by naoe-FOAM-SJTU solver," *Int. J. Ocean Syst. Eng.* **4**(1), 49–56.

Cao, H. J., Wang, X. Y., Liu, Y. C. and Wan, D. C. [2013] "Numerical prediction of wave loading on a floating platform coupled with a mooring system," *Twenty-Third* (2013) *Int. Offshore Polar Eng. Conf.*, Anchorage, Alaska, USA.

Cheng, P., Huang, Y. and Wan, D. [2019] "A numerical model for fully coupled aero-hydrodynamic analysis of floating offshore wind turbine," *Ocean Eng.* **173**, 183–196.

Coulling, A. J., Goupee, A. J., Robertson, A. N., Jonkman, J. M. and Dagher, D. J. [2013] "Validation of a FAST semi-submersible floating wind turbine numerical model with DeepCwind test data," *J. Renew. Sustain. Energy* **5**(2), 023116.

De Boer, A., Van der Schoot, M. S. and Bijl, H. [2007] "Mesh deformation based on radial basis function interpolation," *Comput. Struct.* **85**(11–14), 784–795.

Diaconu, S. [2013] "Wave run-up simulations and comparison with experimental data on a semi-submersible," *Mech. Test. Diagn.* **1**, 32–37.

Dunbar, A. J., Craven, B. A. and Paterson, E. G. [2015] "Development and validation of a tightly coupled CFD/6-DOF solver for floating offshore wind turbine platforms," *Ocean Eng.* **110**, 98–105.

Eymard, R., Gallouët, T. and Herbin, R. [2000] "Finite volume methods," in *Handbook of Numerical Analysis*, Vol. 7, pp. 713–1018.

Fan, T., Qiao, D. and Ou, J. [2012] "Optimized design of equivalent truncated mooring system based on similarity of static and damping characteristics," *Twenty-Second* (*2012*) *Int. Offshore Polar Eng. Conf.*, International Society of Offshore and Polar Engineers.

Fossen, T. [2011] *Handbook of Marine Craft Hydrodynamics and Motion Control* (John Wiley &Sons, Hoboken N.J., USA).

Yong-Pyo, H., Dong-Yeon, L., Yong-Ho, C., Sam-Kwon, H. and Se-Eun, K. [2005] "An experimental study on the extreme motion responses of a spar platform in the heave resonant waves," *Fifteenth* (*2005*) *Int. Offshore Polar Eng. Conf.*, Seoul, Korea.

Huang, Y., Cheng, P. and Wan, D. [2019] "Numerical analysis of a floating offshore wind turbine by coupled aero-hydrodynamic simulation," *J. Mar. Sci. Appl.* **18**(1), 82–92.

Huijs, F., Ridder, E. J. and Savenije, F. [2014] "Comparison of model tests and coupled simulations for a semi-submersible floating wind turbine," *ASME 2014 33th Int. Conf. Ocean, Offshore Arctic Eng.*, June 8–13, San Francisco, California, USA.

Issa, R. I. [1986] "Solution of the implicitly discretised fluid flow equations by operator-splitting," *J. Comput. Phys.* **62**(1), 40–65.

ITTC. ITTC Recommended Procedures — Sea Keeping Experiments. (2002), p. 4.

Jonkman, J. [2007] *Dynamics Modeling and Loads Analysis of an Offshore Floating Wind Turbine* (ProQuest, AnnArbor, Michigan, USA).

Jonkman, J. [2013] *HydroDyn Manual.* NWTC information portal (HydroDyn). Available at https://nwtc.nrel.gov/HydroDyn (accessed 24 July 2015).

Jonkman, J. and Buhl, M. [2005] *FAST Usersguide*. NWTC Information Portal (FASTv8). Available at https://nwtc.nrel.gov/FAST8 (accessed 29 September 2015).

Kim, J. W., Magee, A. and Guan, K. Y. H. [2011] "CFD simulation of flow-induced motions of a multi-column floating platform," *ASME 2011 30th Int. Conf. Ocean, Offshore Arctic Eng.*, American Society of Mechanical Engineers Digital Collection, pp. 319–326.

Koo, B. J., Goupee, A. J., Kimball, R. W. and Lambrakos, K. F. [2014] "Model tests for a floating wind turbine on three different floaters," *J. Offshore Mech. Arct.* **136**(2), 020907.

Lee, C. H. and Newman, J. N. [2006] *WAMIT User Manual*, Versions 6.3, 6.3pc, 6.3 s, 6.3 s-pc (WAMIT, Inc., ChestnutHill, MA, USA).

Lee, Y. W., Incecik, A., Chan, H. S. and Kim, Z. K. [2005] "Design evaluation in the aspects of hydrodynamics on a prototype semi-submersible with rectangular cross-section members," *Fifteenth* (2005) *Int. Offshore Polar Engineering Conf.*, Seoul, Korea.

Lin, P. and Liu, P. L. F. [1999] "Internal wave-maker for Navier-Stokes equations models," *J. Waterw. Port. C-ASCE* **125**(4), 207–215.

Liu, Y., Peng, Y. and Wan, D. [2015] "Numerical investigation on interaction between a semi-submersible platform and its mooring system," *ASME* 2015 34*th Int. Conf. Ocean, Offshore Arctic Eng.*, American Society of Mechanical Engineers, pp. V007T06A071–V007T06A071.

Liu, Y., Xiao, Q., Incecik, A., Peyrard, C. and Wan, D. [2017] "Establishing a fully coupled CFD analysis tool for floating offshore wind turbines," *Renew. Energy* **112**, 280–301.

Luan, C., Gao, Z. and Moan, T. [2013] "Modeling and analysis of a semi-submersible wind turbine with a central tower with emphasis on the brace system," *ASME* 2013 32*nd Int. Conf. Ocean, Offshore Arctic Eng.*, June 9–14, Nantes, France.

Naqvi, S. K. [2012] *Scale Model Experiments on Floating Offshore Wind Turbines*. Master Thesis, Worcester Polytechnic Institute, Worcester, MA 01609, United States.

Ohyama, T. and Nadaoka, K. [1991] "Development of a 'numerical wave tank in nonlinear and irregular wave field with non-reflecting boundaries," *Doboku Gakkai Ronbunshu* **1991**(429), 77–86.

OpenFOAM [2013]. Mesh generation with the snappyHexMesh utility. Available at http://www.openfoam.org/docs/user/snappyHexMesh.php#x26-1510005.4.

Orcaflex Manual, Orcina [2015]. Available at http://www.orcina.com/SoftwareProducts/OrcaFlex/DocumentationOrcaFlex.pdf.

Perez, L. R. [2014] *Design, Testing and Validation of a Scale Model Semisubmersible Offshore Wind Turbine Under Regular/Irregular Waves and Wind Loads*. Master Thesis, University of Strathclyde, Glasgow, UK.

Rho, J. B., Choi, H. S. and Shin, H. S. [2002] "Heave and pitch motions of a spar platform with damping plate," *Twelfth* (2002) *Int. Offshore Polar Engineering Conf.*, International Society of Offshore and Polar Engineers.

Robertson, A., Jonkman, J., Masciola, M., Song, H., Goupee, A., Coulling, A. and Luan, C. [2014] Definition of the semisubmersible floating system for phase II of OC4 (No. NREL/TP-5000-60601). National Renewable Energy Lab. (NREL), Golden, CO (United States).

Robertson, A. N. *et al.* [2017] "OC5 project phase II: Validation of global loads of the DeepCwind floating semisubmersible wind turbine," *Energy Procedia* **137**, 38–57.

Rusche, H. [2002] *Computational Fluid Dynamics of Dispersed Two-Phase Flows at High Phase Fractions*. Doctoral Dissertation, University of London.

Sandner, F., Amann, F. and Azcona, J. [2015] "Model building and scaled testing of 5MW and 10MW semi-submersible floating wind turbines," *EERA DeepWind 2015 Conf.* Trondheim, Norway.

Shan, T., Yang, J., Li, X. and Xiao, L. [2011] "Experimental investigation on wave run-up characteristics along columns and air gap response of semi-submersible platform," *J. Hydrodyn. B* **23**, 625–636.

Shen, Z., Cao, H., Ye, H. and Wan, D. [2012] *Manual of CFD Solver for Ship and Ocean Engineering Flows: naoe-FOAM-SJTU.* Tech. Rep. Solver Man., Shanghai Jiao Tong University.

SIMPACK News Edition July [2013]. Available at http://www.simpack.com/fileadmin/simpack/doc/newsletter/2013/Jul_2013/SN-2013-Jul_all_full-issue_Spreads_HQ150dpi.pdf (accessed on 22 May 2014).

Sun, X., Huang, D. and Wu, G. [2012] "The current state of offshore wind energy technology development," *Energy* **41**(1), 298–312.

Tang, Y. G., Song, K. and Wang, B. [2015] "Experiment study of dynamics response for wind turbine system of floating foundation," *China Ocean Eng.* **29**(6), 835–846.

Tran, T. T. and Kim, D. H. [2015] "The coupled dynamic response computation for a semi-submersible platform of floating offshore wind turbine," *J. Wind Eng. Ind. Aerod.* **147**, 104–119.

Van Leer, B. [1979] "Towards the ultimate conservative difference scheme. V. A second-order sequel to Godunov's method," *J. Comput. Phys.* **32**(1), 101–136.

Vugts, J. H. [1968] *The Hydrodynamic Coefficients for Swaying, Heaving and Rolling Cylinders in a Freesurface.* Technical Report.

Wang, J. and Wan, D. C. [2018] "CFD investigations of ship maneuvering in waves using naoe-FOAM-SJTU Solver," *J. Mar. Sci. Appl.* **17**(3), 443–458.

Wang, J., Zhao, W. and Wan, D.C. [2019] "Development of naoe-FOAM-SJTU solver based on OpenFOAM for marine hydrodynamics," *J. Hydrodyn.* **31**(1), 1–20.

Yang, H. Y., He, E. M. and Zhang, Y. [2015] "Optimization design of TMD for vibration suppression of offshore floating wind turbine," *Int. J. Plant Eng. Manag.* **1**(20), 13–27.

Yu, M., Hu, Z. and Xiao, L. [2015] "Wind-wave induced dynamic response analysis for motions and mooring loads of a spar-type offshore floating wind turbine," *J. Hydrodyn. B* **26**(6), 865–874.

Zhang, X. and Zou, J. [2002] "Coupled effects of risers/supporting guide frames on spar responses," *12th Int. Offshore Polar Engineering Conf.*, Kitakyushu, Japan.

Zhao, W. and Wan, D. [2015] "Numerical study of interactions between phase II of OC4 wind turbine and its semi-submersible floating support system," *J. Ocean Wind Energy* **2**, 45–53.

Zhao, Y., Yang, J., He, Y. and Gu, M. [2016] "Dynamic response analysis of a multi-column tension-leg-type floating wind turbine under combined wind and wave loading," *J. Shanghai Jiaotong Univ. Sci.* **21**(1), 103–111.

Zhuang, Y. and Wan, D. C. [2019] "Numerical simulation of ship motion fully coupled with sloshing tanks by naoe-FOAM-SJTU solver," *Eng. Comput.* **36**(8), 2787–2810.

Zhuang, Y. and Wan, D. C. [2019] "Numerical study of focused waves acting on a fixed FPSO-shaped body," *Int. J. Offshore Polar.* **29**(2), 128–140.